

Sodium citrate-assisted prussian blue analogues as K-rich cathode materials for sodium ion batteries

Peng li (✉ lipeng516@usst.edu.cn)

Taiyuan Institute Of Technology <https://orcid.org/0000-0002-9847-4559>

Genfei Gu

North University of China

Yong Jiang

North University of China

Baoyin Cui

Taiyuan Institute Of Technology

Minrui Sun

North University of China

Shiyou Zheng

University of Shanghai for Science and Technology

Research Article

Keywords: Sodium ion batteries, Cathode, Prussian blue analogs, Nanobox

Posted Date: December 15th, 2021

DOI: <https://doi.org/10.21203/rs.3.rs-1109024/v1>

License:   This work is licensed under a Creative Commons Attribution 4.0 International License.

[Read Full License](#)

Abstract

Prussian blue analogue (PBA), as the cathode material of sodium ion batteries (SIBs), has attracted much attention because of its low price and open three-dimensional channel structure. However, the traditional methods for preparing PBA have high crystallization rate, high water content and many structural defects, which hinder the development of PBA for the application of in batteries. To solve the above problems, in this study, sodium citrate was used to improve the nucleation rate and crystallinity. Herein, PBM₁ synthesized by this method not only has good crystallinity and regular particles, but also shows excellent electrochemical performance when used as cathode in SIBs. Under the current density of 0.05A/g, it has a specific capacity of 109.6 mAh/g. At a current density of 0.1A/g, the reversible specific capacity could keep as high as 95.0 mAh/g and with a coulombic efficiency of almost 100% after 300 cycles.

1. Introduction

The increasingly serious resource shortage and energy crisis have become the biggest obstacle to the rapid development of modern society. In order to meet the significantly increased energy consumption and reduce dependence on non-renewable resources, various types of energy storage systems have been developed, such as lithium-ion batteries (LIB), sodium-ion batteries (SIB) and lithium-sulfur batteries¹. Currently, lithium-ion batteries are the most versatile and considered the most promising energy storage equipment. However, the shortage and expensive price of lithium resources may restrict its further development. Considering the abundance of resources and cost, sodium ion batteries have received widespread attention from society and are considered to be the main energy storage equipment in the future². Nevertheless, several challenges must be overcome to enable sodium-ion batteries to replace or replenish lithium-ion batteries. Especially, compared with lithium ion, the larger radius of sodium ion makes its diffusion speed in active materials slow, resulting in limited rate performance. In addition, during insertion and extraction of sodium ions, the large size radius of sodium ions will easily lead to structural collapse and lattice distortion of materials, resulting in the inhibition of cycling ability³. In order to solve the above problems, the preparation of prussian blue analogs (PBAs) electrode materials is considered to be an effective method due to its inherent open framework structure and large interstitial sites⁴.

As a typical cathode material for sodium ion batteries, the molecular formula of PBAs are $A_xM_\alpha[M_\beta(CN)_6]_{1-y}\cdot zH_2O$, where A are alkali metal ions, M_α and M_β are transition metal ions, \square indicating the vacancy occupied by coordinated water⁵. In the structure of PBA, M_α and M_β transition metal cations are connected with cyanide ions through $M_\alpha-C\equiv N-M_\beta$ bonds, forming an open framework with a large number of interstitial sites^{6, 7}. Due to the different types and contents of alkali metal ions, the types of transition metal ions and the number of vacancies, PBAs electrode materials have different properties. Moreover, the easy synthesis and low cost of PBA materials at room temperature are also very conducive to large-scale applications⁸. However, when PBAs were used as cathode materials of sodium ion batteries in the early stage, the target products were generally synthesized by traditional liquid phase

precipitation method, which had high crystallization rate, high water content and many defects in the structure of the target products, resulting in poor cycle performance^[9]. In order to solve the above problems, citric acid assisted method was adopted in this experiment. Compared with the traditional synthesis method^[10], the obtained material has more perfect crystal structure, fewer defects and lower water content^[11]. As the cathode material of sodium ion battery, it shows high charge-discharge platform, high specific capacity, high-rate performance and high cycle stability. At the same time, in order to effectively prevent the structure and lattice changes caused by sodium ion insertion/extraction, the prepared material must have a large enough gap and a rigid frame. In this experiment, PBA cathode material with rigid hollow nanobox structure was prepared, and alkali metal ion A was changed into potassium ion, which enlarged the gap^[12]. Compared with the inserted/extracted sodium ions, the inner part has a larger gap and a stronger skeleton, which leads to the smallest material structure change and lattice modification during the insertion/extraction of sodium ions.

This work uses the traditional liquid phase method, adding potassium ferricyanide to provide potassium ions and different kinds of transition metal ions (Co^{2+} , Mn^{2+}) salt compounds and adding sodium citrate as an auxiliary agent to synthesize the corresponding potassium-rich hexacyanoferrate salt compounds (PBC, PBZ, PBM)^[13]. Performance tests on several synthesized materials show that potassium-rich manganese hexacyanoferrate has high specific capacity, excellent performance rate and cycle life^[14]. This may be due to PBM cathode material has perovskite structure and hollow nanobox structure, which leads to open three-dimensional network frame structure, large gap position, low water content and few structural defects compared with PBC. And compared with the PBC cathode material, the higher redox potential of PBM leads to the higher discharge voltage platform and the greater energy density^[15].

2. Experimental

2.1 Chemicals

$\text{Co}(\text{NO}_3)_2 \cdot 6\text{H}_2\text{O}$, $\text{Mn}(\text{CH}_3\text{COO})_2 \cdot 4\text{H}_2\text{O}$, $\text{Mn}(\text{NO}_3)_2$, $\text{Na}_3\text{C}_6\text{H}_5\text{O}_7 \cdot 2\text{H}_2\text{O}$ and $\text{K}_3[\text{Fe}(\text{CN})_6]$ were analytical grade without further purification.

2.2 Syntheses of PBA

In the typical synthesis process of K-rich manganese hexacyanoferrate (K-PBM₁), 0.06 mol of $\text{Mn}(\text{CH}_3\text{COO})_2 \cdot 4\text{H}_2\text{O}$ and 0.09 mol of $\text{Na}_3\text{C}_6\text{H}_5\text{O}_7 \cdot 2\text{H}_2\text{O}$ were dissolved into 2 L of deionized water at room temperature to obtain a homogeneous solution (solution A). Then 0.04 mol of $\text{K}_3[\text{Fe}(\text{CN})_6]$ was dissolved in 2 L of deionized water by magnetic stirring at room temperature (solution B). Under vigorous stirring, pouring solution B was poured into solution A to form a homogeneous mixed solution^[16]. After standing at room temperature for 18 h, the precipitate was centrifuged and washed with deionized water and ethanol three times, respectively. Finally, the product was dried in a blast drying oven at 70 °C for 12 h to obtain the K-PBM₁ nanobox. Replace the $\text{Mn}(\text{CH}_3\text{COO})_2 \cdot 4\text{H}_2\text{O}$ mentioned above with $\text{Co}(\text{NO}_3)_2 \cdot 6\text{H}_2\text{O}$,

and the amount of other materials and experimental conditions remain unchanged, and K-PBC is synthesized respectively. At the same time, a control experiment was performed to synthesize K-PBM₂ with Mn(NO₃)₂ instead of Mn(CH₃COO)₂·4H₂O.

2.3 Material characterization

The crystal structure of the powder material was characterized using X-ray diffraction (XRD), on Smart Lab Japan (40 kV, 200 mA, Cu-K_α radiation). The microscopic morphology of the material was observed by using a field-emission scanning electron microscope (SEM) (JSM-7200F, Japan) and a high-resolution transmission electron microscope (TEM, JEOL2100F). The material has been analyzed for surface element and chemical valence state by X-ray photoelectron spectrometer (XPS, ESCALAB250).

2.4 Electrochemical measurements

By mixing electroactive materials (PBA), conductive carbon black (acetylene black), and binder polyvinylidene fluoride (PVDF) in a weight ratio of 7:2:1, add N-methylpyrrolidine in a mortar (NMP) and grind them evenly for about 30 minutes, until they are completely ground into a slurry. After that, the slurry was uniformly coated on the copper foil and dried at 80°C for 12 hours, and then assembled into a CR2025 coin battery. The separator used is glass fiber (GF/D), and the electrolyte is a solution of 1.0M NaPF₆ in EC: DEC = 1: 1 Vol% with 5.0% FEC. At room temperature, the charging and discharging performance of the battery was tested in the voltage range of 2.7-4V through the LAND CT 2001A test system. Cyclic voltammetry (CV) and electrochemical impedance spectroscopy (EIS) were performed on the battery on the CHI760E electrochemical workstation.

3. Results And Discussion

In this experiment, PBAs powder was synthesized by a simple precipitation method.

For K-PBM



For K-PBC



XRD and SEM were carried out to study the phase, composition and micromorphology of the prepared samples, and the results are shown in Fig 1. In the XRD images of all PBA products, the positions of the characteristic diffraction peaks were basically the same and the diffraction peaks were sharp and strong, indicating that these samples had high crystallinity. In addition, in the SEM image as shown in the figs1.c-

e, all of them had regular structure of nanobox. It could be seen that by replacing Fe(II) in $KFe(II)Fe(II)(CN)_6$ with similar transition metal ions such as Mn(II) or Co(II) the products still maintain a cubic framework structure and are arranged in an orderly manner. The XRD patterns of PBM in Fig. 1a were very consistent with the standard card of $KMnFe(CN)_6 \cdot 2H_2O$ (JCPDS 51-1896)^[17]. Moreover, the characteristic peaks of PBM₁ and PBM₂ at 17.5, 24.2, 24.9, 25.4 and 35.4° corresponded to (002), (202), (220), (202) and (040) crystal planes^[18]. Comparing their characteristic peaks, the characteristic peak intensity of PBM₁ is higher and the adjacent impurity peaks are less, indicating that the purity of PBM₁ is purer. The SEM images in Figs. 1c and 1d showed that the product is a nanobox structure. PBM₁ was superior to PBM₂ in terms of regular morphology and uniform size of particles^[19]. As shown in Fig. 1b, the XRD pattern of PBC was very similar to the standard card of $Co_3[Fe(CN)_6]_2 \cdot 10H_2O$ (JCPDS 46-0907). The characteristic peaks at 17.2°, 24.4°, 34.8°, 39.1°, 43.0°, 50.1°, 53.3°, 56.5°, and 68.1° are assigned to (200), (220), (400), (420), (422), (440), (600), (620) and (642) planes^[17], respectively. Fig. 1e shows the SEM image of PBC, which clearly shows the nanobox structure with a particle size of about 400 nm. Compared with the three samples, PBC is the smallest of the three, followed by PBM₁. In addition, unobtrusive peaks can also be found in XRD patterns, indicating that the prepared samples have superior crystallinity, which is related to the slow nucleation process controlled with the assistance of sodium citrate.

Energy dispersive X-ray spectroscopy (EDX) was performed on the PBA sample to determine the proportion of each element. The analysis report in Fig. 2a shows that the ratio of k: Mn: Fe: O is 1.43: 1: 0.85: 0.16. Therefore, the molecular formula of PBM₁ can be determined as $K_{1.43}Mn[Fe(CN)_6]_{0.85} \cdot 0.16H_2O$ according to these measurement results. Through similar operations, the molecular formula of PBM₂ is $K_{1.51}Mn[Fe(CN)_6]_{0.91} \cdot 0.05H_2O$ and PBC is $K_{0.41}Co[Fe(CN)_6]_{0.72}$. The morphology and microstructure of the obtained samples were further characterized by TEM. TEM images (Figs. 3a, 3c and 3e) showed that all PBA successfully prepared hollow nanoboxes. These nanospheres have an advanced hollow box structure, which can provide more active sites and faster diffusion channels, thereby obtaining higher ion diffusion kinetics and excellent electrochemical performance^[20]. As depicted in Figs. 3b, 3d and 3f, the distribution range of K, Mn(Co), Fe, C and N fell uniformly in the hollow nanoboxes^[21]. Combined with XRD, SEM, EDX and TEM data, it can be confirmed that the nanoboxes with hollow structure has been successfully prepared. Unlike the smooth surface of PBC naobox, the rough surfaces of PBM₁ and PBM₂ nanobox can effectively provide a large number of active sites and diffusion pathways. Different from the irregular and uneven nanoboxes of PBM₂, the box structure of PBM₁ is more perfect. It can't be ignored that the shell thickness of the sample is extremely important, because the thicker shell will introduce impurities, while the thinner shell may cause instability of the hollow box skeleton^[22]. It can be clearly observed from the figure that compared with PBM₂ and PBC, the shell thickness of PBM₁ is between them, and the thickness is moderate.

In order to further determine the elemental composition, chemical valence and electronic state of PBA materials, the samples were characterized by XPS. XPS spectra of PBM₁ are shown in Figs. 4(a-c). Full spectrum (Fig. 4a) contains Mn2p, Fe2p, C1s, K2p and N1s peaks. As shown in Fig. 4b, in the high

resolution XPS spectrum of Mn 2p, the peaks at 641.8 and 653.7 eV are designated as Mn 2p_{3/2} and Mn 2p_{1/2}, which are directly divided into two corresponding sub-peaks, and a satellite peak appears at 645.6 eV in the middle, indicating that the valence state of Mn in the sample is only positive divalent. Accordingly, in Fig. 4c, the spectrum shows that the peaks of Fe2p_{3/2} and 2p_{1/2} appear at 708.6 eV and 721.6 eV, and the corresponding sub-peaks have no satellite peaks, which belong to Fe²⁺ in [Fe(CN)₆]⁴⁺ and Fe³⁺ in [Fe(CN)₆]³⁺, respectively^[23]. It is worth noting that the orbital peaks and binding energies in the fitting curves of Fe2p in the three samples are in the same position, which confirms the existence of iron cyanide ions. The elements displayed in the scanning spectrum (Fig. 4d) of PBM₂ correspond to PBM₁ one by one, and the fitting curve of its Fig. 4e Mn2p is basically consistent with that of Fig. 4b, except that the position where binding energy appears changes slightly. The above proves the successful preparation of PBM materials. The scanning spectrum of PBC (Fig. 4g) includes Mn2p, Fe2p, C1s, K2p and N1s peaks. As shown in Fig. 4f, it can be observed that the binding energies of Co2p_{1/2} and Co2p_{3/2} appear at 779.7 and 782.4eV, and there is a satellite peak at 786.7eV in the middle, which reveals the existence of Co²⁺, combined with the spectrum of Fe2p (Fig. 4g) can be proved the successful synthesis of PBC materials^[24].

In order to understand the electrochemical properties of the prepared materials, cyclic voltammetry and rate tests were carried out. Fig. 5a shows the first three cyclic voltammetry curves of PBM₁ in the potential range of 2.0-4.0 V and the scan rate of 0.1 mV s⁻¹. The reduction/oxidation peaks distributed at 3.68/4.13 V and 3.93/4.25 V could be assigned to the Fe³⁺/Fe²⁺ and Mn³⁺/Mn²⁺, respectively. The phenomenon of these overlapping of PBM1 indicates the excellent reversibility of sodium ion. It could be observed two symmetrical oxidation/reduction peaks at 3.36/3.18 V in the first cycle, corresponding to the extraction and insertion of Na⁺. From the second cycle, the oxidation-reduction peak (3.32/3.19 V) was well maintained suggested the highly reactive reversibility and good structural stability²⁵. Fig. 5b shows the rate curve at a current density of 0.05 to 1 A/g. At current densities of 0.05, 0.1, 0.2, 0.5 and 1 A/g, the reversible discharge specific capacities of the PBM1 cathode are 109.6, 95.0, 71.1, 38, and 19.1 mAh/g, respectively. At a large current density of 0.5 A/g, 64% of the initial specific capacity can still be maintained. When the current density goes back to 0.05 A/g again, the reversible discharge specific capacity is 114.1 mAh/g, indicating that PBM₁ has superior rate performance. The reversible discharge specific capacities of PBM₂ at current densities of 0.05, 0.1, 0.2, 0.5 and 1 A g⁻¹ are 65.4, 51.6, 33.5, 17.8 and 11.1 mAh/g, respectively. At a large current density of 0.5 A/g, the specific capacity is only 27% of the initial value. When the current density goes back to 0.05 A/g again, the reversible discharge specific capacity is 69.1 mAh/g, and the overall performance is inferior to PBM₁. As for PBC, there is almost no reversible specific capacity at a current density of 0.05-1A/g without further discussion. The reason for the extremely low energy storage performance of the PBC cathode may be that the content of K⁺ in the PBC material is too small, which is only 0.41, far less than 1.43 of PBM₁ and 1.51 of PBM₂. There is no large amount of free K⁺ movement inside, so that the number and size of the material gap points are not up to the standard. At the same time, the smooth surface of its microscopic nanobox cannot provide

sufficient active gap points and diffusion pathways^[26]. The last point is that its thinner shell thickness causes the hollow skeleton to be not strong enough. Comparing the charge/discharge curves of PBM₁ (Fig. 5c) and PBM₂ (Fig. 5d), noticed that although both are charged/ discharged with constant current at a voltage of 2.0-4.0 V. The initial charging voltage of PBM₁ is around 2.5 V and the voltage of PBM₂ is 2.75 V, and the initial discharge voltage is the same. The lower initial charging voltage may be the reason why the rate performance of PBM₁ surpass PBM₂. In order to have a deeper understanding of the electrochemical performance of the PBM cathode, the cycling and impedance performance of PBM₁ and PBM₂ were tested. Fig. 6a is the cycle performance curve of the PBM cathode material at a current density of 0.1A/g. The initial reversible specific capacity of PBM₁ is 75.1 mAh/g, and the highest specific capacity is 91.1 mAh/g. After 300 cycles of charging and discharging, the specific capacity is 75.4 mAh/g, which has no attenuation compared with the initial specific capacity and can still maintain the highest specific capacity of 82%, which proves that PBM₁ has excellent cycle performance^[27]. The initial specific capacity of PBM₂ is 60 mAh/g, and the highest is 69.0 mAh/g. The specific capacity after 300 cycles is 42.2 mAh/g, which is 30% attenuated compared with the initial specific capacity, which is equivalent to the highest specific capacity of 61%. Comparing the cycle charge and discharge curves of PBM₁ (Fig. 6b) and PBM₂ (Fig. 6c), the initial discharge voltage of PBM₁ during each cycle of 300 cycles is about 2.5V, which is lower than the 2.75V of PBM₂. This phenomenon also appears in the rate performance, which is more certain that this is why the electrochemical performance of PBM₁ is superior. In addition, since the energy storage capacity of the electrode material is directly related to its impedance, in order to compare the reaction kinetics of the PBM₁ and PBM₂ electrodes, electrochemical impedance spectroscopy analysis was carried out. The frequency spectrum is shown in Figure 6(b). A concave semicircle is formed in the high frequency area and the middle frequency area, and a straight line is formed in the low frequency area. The semicircle in the high-frequency region and the long diagonal line in the low-frequency region correspond to the charge transfer process and the Warburg diffusion process, respectively. Obviously, the charge transfer resistance (R_{ct}) of PBM₁ is lower, which is more conducive to Na⁺ and electron migration. The reason why the electrochemical performance of PBM₁ is better than that of PBM₂ is that the electrode material of PBM₁ has higher purity, more regular particles and more suitable shell thickness. After characterizing the physical and electrochemical properties of the three electrode materials, the results show that Mn²⁺ is easier to combine with potassium ions to form a rough surface, and acetate ions can form uniform particle and shell thickness^[28].

4. Conclusion

In summary, the PBM (KMnFe(CN)₆) electrode material with high crystallinity rich in K ions and the PBC (Mn₂[Fe(CN)₆]₂) electrode material with a small amount of K⁺ were prepared by a simple and convenient liquid phase precipitation method assisted by sodium citrate. The prepared electrode material well retains the hollow nanobox structure, in which a large amount of K⁺ inside makes the box rough and provides more and larger active sites and diffusion channels to form a more open framework. In addition, the

control experiments show that acetate and Mn^{+} are more likely to form electrode materials high purity, regular particles, rough surface and moderate shell thickness. Open structure, rough surface, high purity, uniform particles and proper shell thickness make PBM_1 have remarkable electrochemical performance, showing a specific capacity of 109.6 mAh/g at a current density of 0.05A/g and long-cycle stability at 0.1 A/g. We believe that the strategy of increasing the nucleation rate and crystallinity with the assistance of sodium citrate and increasing the K^{+} content will make PBA a promising cathode material for SIBs.

Declarations

Compliance with Ethical Standards

Finding: The research was supported by the financial support of: Natural Science Fund of China (51971146), the Fund for “Scientific and Technological Innovation Programs of Higher Education Institutions in Shanxi” (2020L6026) and Research Project Supported by Technology Foundation for Selected Overseas Chinese Scholar (20191176), “Research Project Supported by Shanxi Scholarship Council of China(2020147).”

Conflict of Interest: The authors declare that they have no conflict of interest

References

1. Zhang, S.; Zhang, Y.; Shao, G.; Zhang, P. Bio-inspired construction of electrocatalyst decorated hierarchical porous carbon nanoreactors with enhanced mass transfer ability towards rapid polysulfide redox reactions. *Nano Research* 2021, *14*, 3942–3951.
2. Qian, J.; Wu, C.; Cao, Y.; Ma, Z.; Huang, Y.; Ai, X.; Yang, H. Prussian Blue Cathode Materials for Sodium-Ion Batteries and Other Ion Batteries. *Advanced Energy Materials* 2018, *8*, 1702619
3. Huang, Y.; Xie, M.; Wang, Z.; Jiang, Y.; Yao, Y.; Li, S.; Li, Z.; Li, L.; Wu, F.; Chen, R. A Chemical Precipitation Method Preparing Hollow-Core-Shell Heterostructures Based on the Prussian Blue Analogs as Cathode for Sodium-Ion Batteries. *Small* 2018, *14*, e1801246.
4. Baster, D.; Kondracki, Ł.; Oveisi, E.; Trabesinger, S.; Girault, H. H. Prussian Blue Analogue—Sodium—Vanadium Hexacyanoferrate as a Cathode Material for Na-Ion Batteries. *ACS Applied Energy Materials* 2021, *4*, 9758–9765.
5. Zhu, Y.; Zhang, Z.; Bao, J.; Zeng, S.; Nie, W.; Chen, P.; Zhou, Y.; Xu, Y. Multi-metal doped high capacity and stable Prussian blue analogue for sodium ion batteries. *International Journal of Energy Research* 2020, *44*, 9205–9212.
6. Yu, S.; Li, Y.; Lu, Y.; Xu, B.; Wang, Q.; Yan, M.; Jiang, Y. A promising cathode material of sodium iron–nickel hexacyanoferrate for sodium ion batteries. *Journal of Power Sources* 2015, *275*, 45–49.
7. Phadke, S.; Mysyk, R.; Anouti, M. Effect of cation (Li^{+} , Na^{+} , K^{+} , Rb^{+} , Cs^{+}) in aqueous electrolyte on the electrochemical redox of Prussian blue analogue (PBA) cathodes. *Journal of Energy Chemistry* 2020, *40*, 31–38.

8. Bie, X.; Kubota, K.; Hosaka, T.; Chihara, K.; Komaba, S. Synthesis and electrochemical properties of Na-rich Prussian blue analogues containing Mn, Fe, Co, and Fe for Na-ion batteries. *Journal of Power Sources* 2018, *378*, 322–330.
9. Heli, H.; Majdi, S.; Sattarahmady, N. Fe₂O₃ core–NaCo[Fe(CN)₆] shell nanoparticles—Synthesis and characterization. *Materials Research Bulletin* 2010, *45*, 850–858.
10. Xiao, P.; Song, J.; Wang, L.; Goodenough, J. B.; Henkelman, G. Theoretical Study of the Structural Evolution of a Na₂FeMn(CN)₆ Cathode upon Na Intercalation. *Chemistry of Materials* 2015, *27*, 3763–3768.
11. Yang, D.; Xu, J.; Liao, X. Z.; He, Y. S.; Liu, H.; Ma, Z. F. Structure optimization of Prussian blue analogue cathode materials for advanced sodium ion batteries. *Chem Commun (Camb)* 2014, *50*, 13377–13380.
12. You, Y.; Wu, X.-L.; Yin, Y.-X.; Guo, Y.-G. A zero-strain insertion cathode material of nickel ferricyanide for sodium-ion batteries. *Journal of Materials Chemistry A* 2013, *1*, 14061–14065.
13. Okubo, M.; Li, C. H.; Talham, D. R. High rate sodium ion insertion into core-shell nanoparticles of Prussian blue analogues. *Chem Commun (Camb)* 2014, *50*, 1353–1355.
14. Tang, X.; Liu, H.; Su, D.; Notten, P. H. L.; Wang, G. Hierarchical sodium-rich Prussian blue hollow nanospheres as high-performance cathode for sodium-ion batteries. *Nano Research* 2018, *11*, 3979–3990.
15. Wu, X.; Wu, C.; Wei, C.; Hu, L.; Qian, J.; Cao, Y.; Ai, X.; Wang, J.; Yang, H. Highly Crystallized Na₂CoFe(CN)₆ with Suppressed Lattice Defects as Superior Cathode Material for Sodium-Ion Batteries. *ACS Appl Mater Interfaces* 2016, *8*, 5393–5399.
16. Huang, Y.; Xie, M.; Zhang, J.; Wang, Z.; Jiang, Y.; Xiao, G.; Li, S.; Li, L.; Wu, F.; Chen, R. A novel border-rich Prussian blue synthesized by inhibitor control as cathode for sodium ion batteries. *Nano Energy* 2017, *39*, 273–283.
17. Sottmann, J.; Bernal, F. L. M.; Yuseenko, K. V.; Herrmann, M.; Emerich, H.; Wragg, D. S.; Margadonna, S. In operando Synchrotron XRD/XAS Investigation of Sodium Insertion into the Prussian Blue Analogue Cathode Material Na_{1.32}Mn[Fe(CN)₆]·0.83·zH₂O. *Electrochimica Acta* 2016, *200*, 305–313.
18. Ren, W.; Qin, M.; Zhu, Z.; Yan, M.; Li, Q.; Zhang, L.; Liu, D.; Mai, L. Activation of Sodium Storage Sites in Prussian Blue Analogues via Surface Etching. *Nano Lett* 2017, *17*, 4713–4718.
19. Ma, Q.; Dong, R.; Liu, H.; Zhu, A.; Qiao, L.; Ma, Y.; Wang, J.; Xie, J.; Pan, J. Prussian blue analogue-derived Mn–Fe oxide nanocubes with controllable crystal structure and crystallinity as highly efficient OER electrocatalysts. *Journal of Alloys and Compounds* 2020, *820*, 153438.
20. Kang, Y.; Wang, S.; Hui, K. S.; Li, H. F.; Liang, F.; Wu, X. L.; Zhang, Q.; Zhou, W.; Chen, L.; Chen, F.; Hui, K. N. [Fe(CN)₆] vacancy-boosting oxygen evolution activity of Co-based Prussian blue analogues for hybrid sodium-air battery. *Materials Today Energy* 2021, *20*, 100572.
21. Wheeler, S.; Capone, I.; Day, S.; Tang, C.; Pasta, M. Low-Potential Prussian Blue Analogues for Sodium-Ion Batteries: Manganese Hexacyanochromate. *Chemistry of Materials* 2019, *31*, 2619–

2626.

22. Xie, B.; Wang, L.; Li, H.; Huo, H.; Cui, C.; Sun, B.; Ma, Y.; Wang, J.; Yin, G.; Zuo, P. An interface-reinforced rhombohedral Prussian blue analogue in semi-solid state electrolyte for sodium-ion battery. *Energy Storage Materials* 2021, *36*, 99–107.
23. Wang, J.-G.; Zhang, Z.; Liu, X.; Wei, B. Facile synthesis of cobalt hexacyanoferrate/graphene nanocomposites for high-performance supercapacitor. *Electrochimica Acta* 2017, *235*, 114–121.
24. Jiang, J.; Tian, H.; He, X.; Zeng, Q.; Niu, Y.; Zhou, T.; Yang, Y.; Wang, C. A CoHCF system with enhanced energy conversion efficiency for low-grade heat harvesting. *Journal of Materials Chemistry A* 2019, *7*, 23862–23867.
25. Jiang, X.; Zhang, T.; Yang, L.; Li, G.; Lee, J. Y. A Fe/Mn-Based Prussian Blue Analogue as a K-Rich Cathode Material for Potassium-Ion Batteries. *ChemElectroChem* 2017, *4*, 2237-2242.
26. Levin, E. E.; Kokin, A. A.; Presnov, D. E.; Borzenko, A. G.; Vassiliev, S. Y.; Nikitina, V. A.; Stevenson, K. J. Electrochemical Analysis of the Mechanism of Potassium-Ion Insertion into K-rich Prussian Blue Materials. *ChemElectroChem* 2020, *7*, 761-769.
27. Huang, T.; Du, G.; Qi, Y.; Li, J.; Zhong, W.; Yang, Q.; Zhang, X.; Xu, M. A Prussian blue analogue as a long-life cathode for liquid-state and solid-state sodium-ion batteries. *Inorganic Chemistry Frontiers* 2020, *7*, 3938–3944.
28. Zhou, A.; Xu, Z.; Gao, H.; Xue, L.; Li, J.; Goodenough, J. B. Size-, Water-, and Defect-Regulated Potassium Manganese Hexacyanoferrate with Superior Cycling Stability and Rate Capability for Low-Cost Sodium-Ion Batteries. *Small* 2019, *15*, e1902420.

Scheme

Scheme 1 is available in the Supplemental Files section

Figures

Figure 1

XRD patterns and SEM of the PBA: (a) XRD patterns of PBM₁; (b) XRD pattern of PBC; (c) SEM image of PBM₁; (d) SEM image of PBM₂; (e) SEM image of PBC.

Figure 2

EDX patterns of the PBA: (a) PBM₁; (b) PBM₂; (c) PBC.

Figure 3

TEM images of (a) PBM₁; (c) PBM₂; (e) PBC; and elemental mapping distribution for (b) PBM₁; (d) PBM₂; (f) PBC.

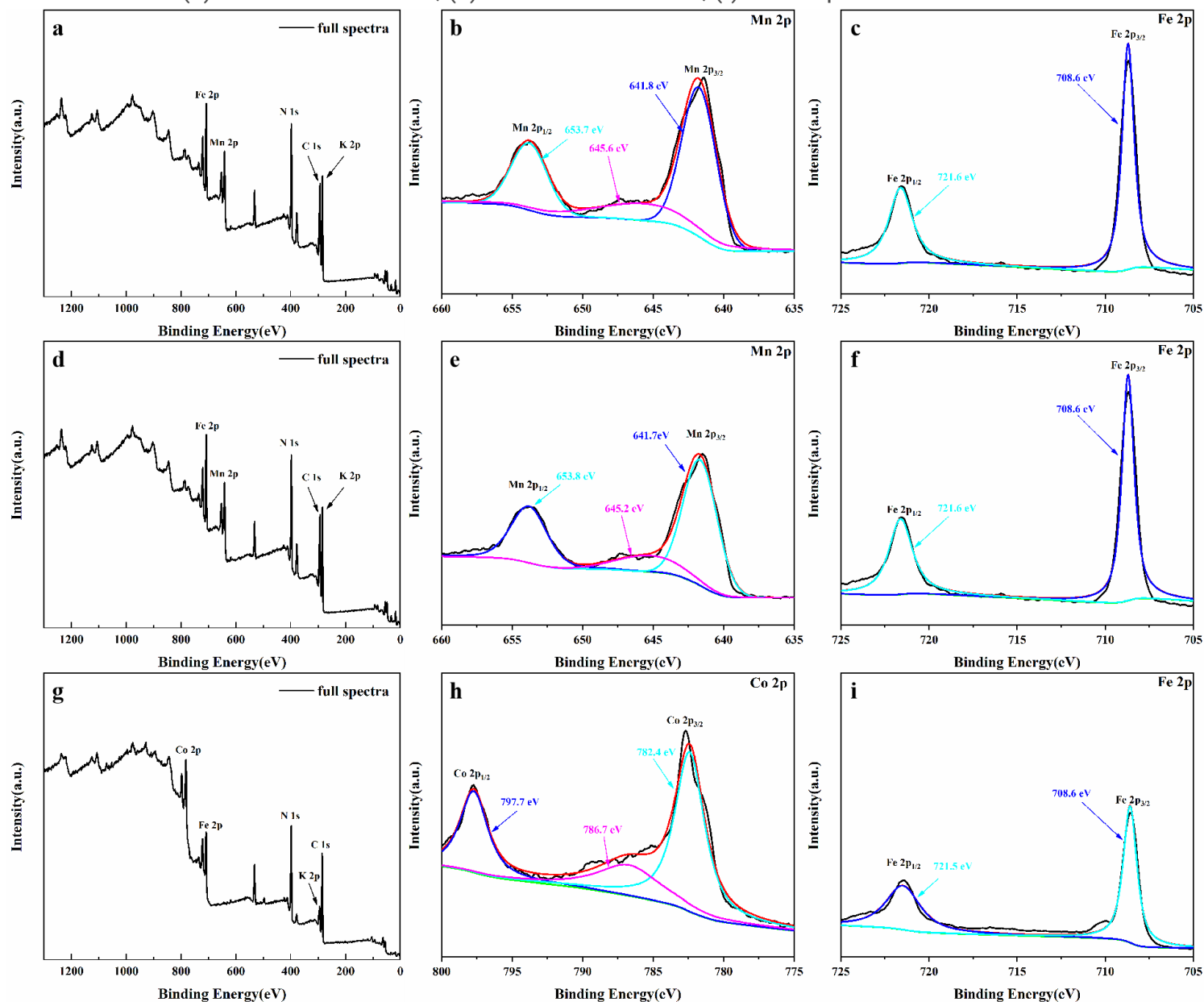


Figure 4

Typical XPS of (a) PBM₁: (b) Mn2p; (c) Fe2p; (d) PBM₂: (e) Mn2p; (f) Fe2p; and (g) PBM₁: (h) Co2p; (i) Fe2p.

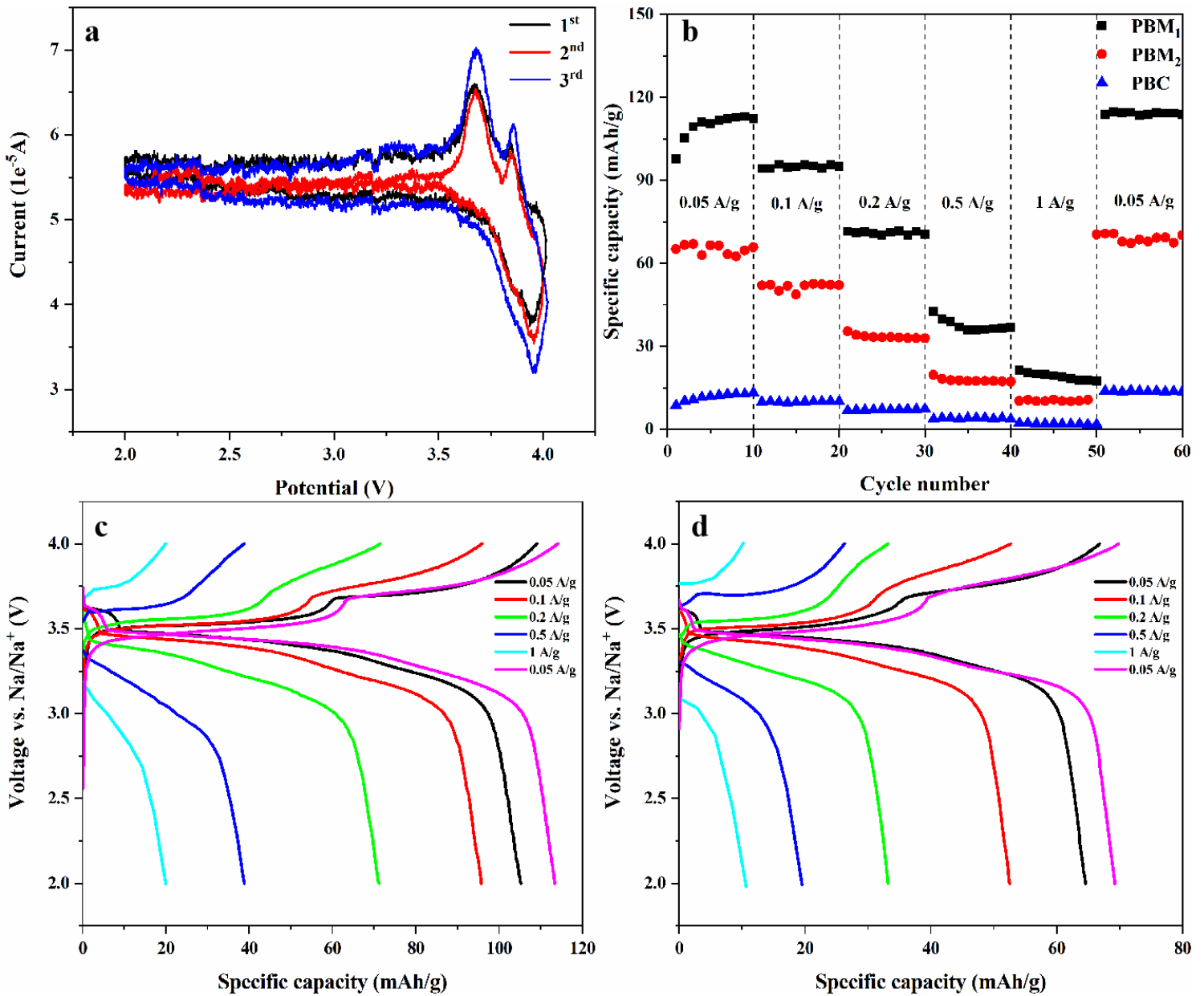


Figure 5

Electrochemical performance characterization of PBA samples in button SIBs. (a) Cyclic voltammetry curves of the first three cycles of PBM₁. (b) The rate capability of PBM₁, PBM₂ and PBC at different current densities. (c-d) The charge/discharge curves of PBM₁ and PBM₂ at different current densities.

Figure 6

(a) Cyclic performance curve at current density of 0.1 A/g. (b) Characteristic impedance spectra (Nyquist plots) of PBM₁ and PBM₂. (c-d) Different cycle charge/discharge curves of PBM₁ and PBM₂ at a current density of 0.1 A/g.

Supplementary Files

This is a list of supplementary files associated with this preprint. Click to download.

- [Scheme1.png](#)